Astronomy & Astrophysics manuscript no.
(DOI: will be inserted by hand later)
March 30, 2006

A quantitative comparison between Type Ia supernova spectra at low and high redshifts.

G. Garavini[1,4], G. Folatelli[2], S. Nobili[1], G. Aldering[3], R. Amanullah[1], P. Antilogus[4], P. Astier[4], G. Blanc[5], J. Bronder[6], M. S. Burns[7], A. Conley[3,8], S. E. Deustua[9], M. Doi[10], S. Fabbro[11], V. Fadeyev[3], R. Gibbons[12], G. Goldhaber[3,8], A. Goobar[1], D. E. Groom[3], I. Hook[6], D. A. Howell[13], N. Kashikawa[14], A. G. Kim[3], M. Kowalski[3], N. Kuznetsova[3], B. C. Lee[3], C. Lidman[15], J. Mendez[16,17], T. Morokuma[10], K. Motohara[10], P. E. Nugent[3], R. Pain[4], S. Perlmutter[3,8], R. Quimby[3], J. Raux[4], N. Regnault[4], P. Ruiz-Lapuente[17], G. Sainton[4], K. Schahmaneche[4], E. Smith[12], A. L. Spadafora[3], V. Stanishev[1], R. C. Thomas[3], N. A. Walton[18], L. Wang[3], W. M. Wood-Vasey[3,8], and N. Yasuda[19]

(The Supernova Cosmology Project)

[1] Department of Physics, Stockholm University, Albanova University Center, S-106 91 Stockholm, Sweden
[2] Observatories of the Carnegie Institution of Washington, 813 Santa Barbara St., Pasadena, CA 91101
[3] E. O. Lawrence Berkeley National Laboratory, 1 Cyclotron Rd., Berkeley, CA 94720, USA
[4] LPNHE, CNRS-IN2P3, University of Paris VI & VII, Paris, France
[5] Osservatorio Astronomico di Padova, INAF, vicolo dell'Osservatorio 5, 35122 Padova, Italy
[6] Department of Physics, University of Oxford, Nuclear & Astrophysics Laboratory, Keble Road, Oxford, OX1 3RH, UK
[7] Colorado College, 14 East Cache La Poudre St., Colorado Springs, CO 80903
[8] Department of Physics, University of California Berkeley, Berkeley, 94720-7300 CA, USA
[9] American Astronomical Society, 2000 Florida Ave, NW, Suite 400, Washington, DC, 20009 USA.
[10] Institute of Astronomy, School of Science, University of Tokyo, Mitaka, Tokyo, 181-0015, Japan
[11] CENTRA e Dep. de Fisica, IST, Univ. Tecnica de Lisboa
[12] Department of Physics and Astronomy, Vanderbilt University, Nashville, TN 37240, USA
[13] Department of Astronomy and Astrophysics, University of Toronto, 60 St. George St., Toronto, Ontario M5S 3H8, Canada
[14] National Astronomical Observatory, Mitaka, Tokyo 181-0058, Japan
[15] European Southern Observatory, Alonso de Cordova 3107, Vitacura, Casilla 19001, Santiago 19, Chile
[16] Isaac Newton Group, Apartado de Correos 321, 38780 Santa Cruz de La Palma, Islas Canarias, Spain
[17] Department of Astronomy, University of Barcelona, Barcelona, Spain
[18] Institute of Astronomy, Madingley Road, Cambridge CB3 0HA, UK
[19] Institute for Cosmic Ray Research, University of Tokyo, Kashiwa, 277 8582 Japan

Abstract. We develop a method to measure the strength of the absorption features in Type SNe Ia spectra and use it to make a quantitative comparison between the spectra of Type Ia supernova at low and high redshifts. Through the strength of these features and through measurements of the Ca II H and K velocity we show that the spectra of a high redshift sample, consisting of 12 SNe Ia with redshifts ranging from 0.212 to 0.912, are quantitatively similar to the spectra of a low redshift sample. One supernova in our high redshift sample, SN 2002fd at z=0.279, is found to have spectral characteristics that are associated with peculiar SN 1991T/SN 1999aa-like supernovae.

1. Introduction

Type Ia supernovae (SNe Ia) are excellent distance indicators and have been used to show that the expansion of the Universe is currently accelerating (Perlmutter et al. 1998; Garnavich et al. 1998; Schmidt et al. 1998; Riess et al. 1998; Perlmutter et al. 1999; Knop et al. 2003; Tonry et al. 2003; Barris et al. 2004; Riess et al. 2004).

Recently, both the SNLS[1] and ESSENCE[2] projects, which use hundreds of SNe Ia to constrain the nature of dark energy through the measurement of the equation of state parameter, have reported their first results. The control of the systematic uncertainties is critical to their success. Among the possible systematic effects, evolution of the SNe Ia population over cosmological time-scales is one of the most important.

Send offprint requests to: G. Garavini , gabri@physto.se

[1] http://www.cfht.hawaii.edu/SNLS/
[2] http://www.ctio.noao.edu/essence/

The spectral energy distribution provides an avenue for quantifying this. For example, the average metallicity of the Universe increases with cosmic time, so it is not unreasonable to expect that high-redshift SNe Ia are in environments that have lower average metallicity. The effect on the spectral energy distribution of a lower metallicity progenitor has been modeled by Hoeflich et al. (1998) and Lentz et al. (2000). These studies find that such SNe Ia, especially at early epochs, are expected to show enhanced flux in the UV, weaker absorption features in the optical and a shift in the minima of optical features to redder wavelengths.

With the large number of well-observed low-redshift supernovae now available, a wide range of spectral diversities is being found (see e.g Branch (2003)). The physical origin of these differences is still not completely understood making it difficult to predict their possible drift as a function of redshift. Statistical studies are useful to probe for differences between high and low-redshift SN data sets. So far, very few distant SN Ia spectra have been compared with low-redshift data sets in a systematic manner (Perlmutter et al. 1998; Coil et al. 2000; Barris et al. 2004; Riess et al. 2003; Blakeslee et al. 2003; Matheson et al. 2005; Hook et al. 2005; Balland et al. 2006). Moreover, very few spectroscopically confirmed high-redshift SNe Ia have been reported as peculiar, even though the number of high-redshift SNe Ia spectra that is publicly available now approaches one hundred. In a distance limited survey, Li et al. (2001b,a) find that approximately 20% of all nearby SNe Ia can be classified as SN 1991T/SN 1999aa-like (hereafter we follow the convention of Li et al. (2001b) when describing 91T/99aa-like SNe by using 99Taa to represent this SN subtype), a peculiar, over-luminous SNe Ia. The lack of these SNe in high redshift surveys may be partly due to the difficulty in identifying such SNe in what are generally low S/N spectra. Alternatively, it could be a sign of evolution. The identification of peculiar SNe Ia in high-redshift samples is an important step towards determining whether the range of SNe Ia sub-types that are observed at low redshift is also observed at high redshifts.

During 2000, 2001 and 2002, the Supernova Cosmology Project (SCP) obtained the spectra of 20 high-redshift SNe Ia with FORS2 on the ESO Very Large Telescope (Lidman et al. 2005). In this paper, we analyze the 14 spectra with the highest signal-to-noise ratios and we perform a quantitative comparison between these spectra and the spectra of low-redshift SNe. We also develop an approach to identify SN Ia sub-types at $z \sim 0.5$. The paper is organized as follows. The data set and identification scheme are presented in section 2. The properties of a newly introduced spectral indicator for Type Ia supernovae, i.e. equivalent width, are discussed in section 3. The comparison of high and low-redshift SNe are presented in section 4 together with a statistical analysis of the results. Summary and conclusions are given in section 5

2. Data set and Supernova Identification

2.1. The high-redshift spectroscopic data set

The supernova spectra that are analyzed in this work were obtained as part of several campaigns by the SCP to discover and follow a large number of SNe Ia over a wide range of redshifts. Out of the 20 spectrally confirmed SNe Ia in Lidman et al. (2005), we select the 12 SNe Ia (z=0.212-0.912) with the highest signal-to-noise ratios (S/N per 20 Å resolution element greater than 3) to pursue the quantitative analysis that is presented in section 4. One supernova, SN 2001go, was observed at three epochs, so there are 14 spectra in total.

The biases affecting this sample are complex and we make no attempt to correct the sample for these biases. We briefly mention the strongest ones. First, supernova searches are magnitude limited, so it is unlikely that low-luminosity, SN 1991bg-like SNe will be found. Second, it is more difficult to spectrally confirm high-redshift SNe Ia in spectra where host galaxy contamination is above 75% (Lidman et al. 2005; Howell et al. 2005). Although this affects all SNe Ia to some degree, SNe Ia in bright ellipticals, which tend to have lower luminosities, will be affected most. Moreover, we can not exclude that the signal to noise cut we performed while choosing the subsample of spectra to study did not introduce an extra selection bias toward over-luminous objects. As it will be clear in section 3, the spectral indicators we use to search for evolution with redshift discern only marginally between normal and over-luminous SN Ia. The additional scatter that would be introduced by using data with lower signal-to-noise ratios would obfuscate the result.

The spectra, re-binned to 20 Å per pixel, are shown in Fig. 1, and the properties are summarized in Table 1. A full description of the observations and the data reduction are given in Lidman et al. (2005). Special care was taken in estimating the statistical error spectrum which was estimated from regions free of SN and host galaxy light on the sky-subtracted two dimensional spectrum. The error spectrum is used to estimate the statistical uncertainties on the quantities we compute in the following analysis.

High-redshift supernova spectra usually suffer from host galaxy contamination. On the 2d spectra, the host galaxy and the SN Ia are usually spatially unresolved, making it difficult to estimate the contribution of the host to the observed flux. We estimated this contribution using a template matching technique based on a large set of nearby supernovae spectra and galaxy models similar to those used in Lidman et al. (2005). The contribution of the galaxy light, relative to the total observed flux, are tabulated in column 10 of Table 1.

The epochs with respect to the $B-$band maximum light — reported in Table 1 — were estimated using the preliminary light curve, if available, and/or spectroscopic dating by template matching with low-z SNe. The two methods usually agree within three days (Hook et al. 2005; Howell et al. 2005), therefore we take 3 days to be the uncertainty on the quoted epoch whenever a light curve estimate of the maximum was not available. The redshift of the supernova, when quoted with 3 significant figures, was estimated from host galaxy lines visible in the spectrum. When this was not possible, the redshift was estimated from supernova spectral features, and is then quoted with 2 significant figures to account for a range of SN photospheric velocities.

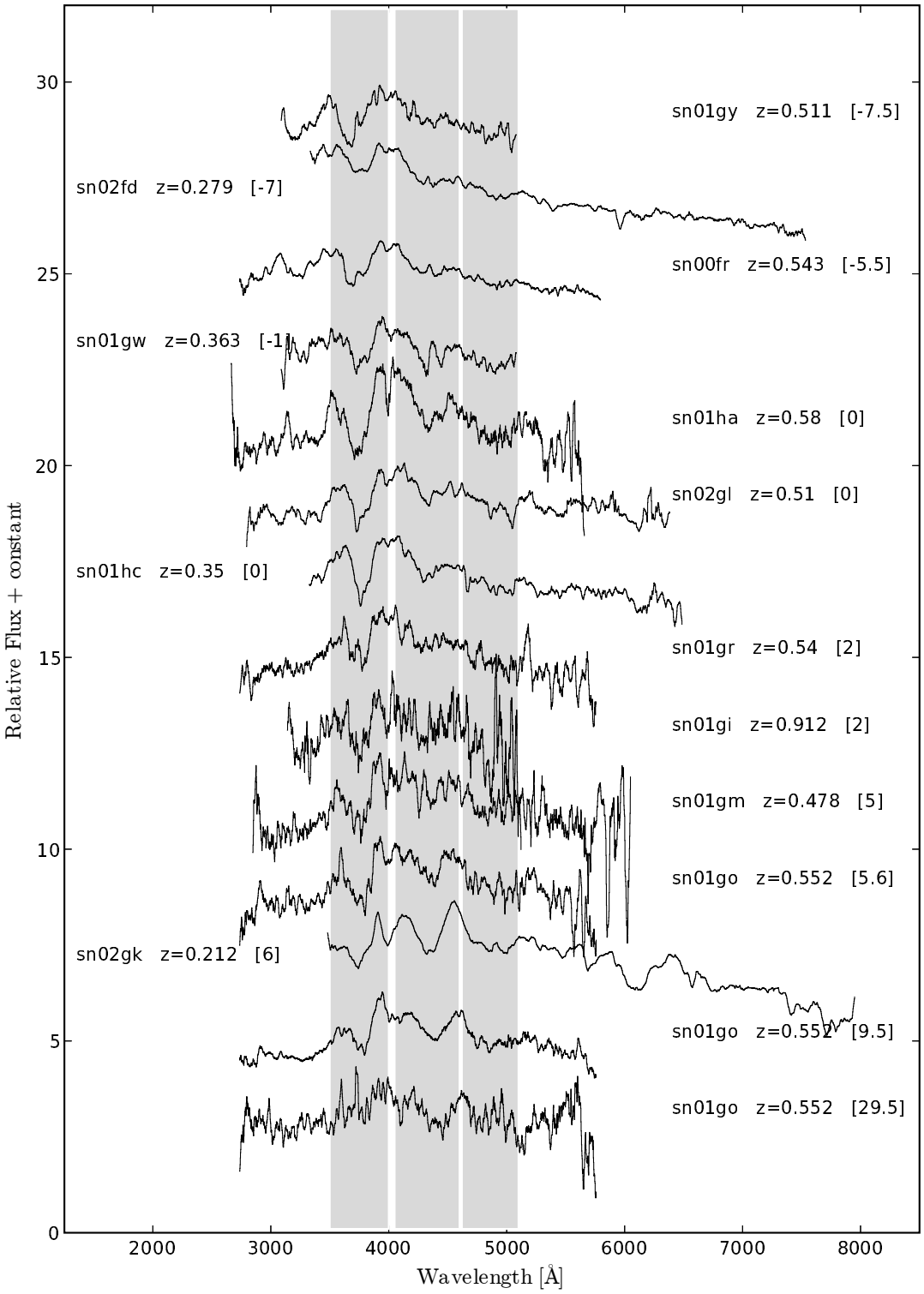

Fig. 1 The spectra of the high-redshift SNe Ia. Name, redshift and epoch (between brackets) label each spectrum shown in the figure. Each spectrum is the original observed spectrum re-binned to 20 Å per pixel and blueshifted to rest frame. See also Table 1 for details. Gray vertical bands indicate the wavelength region used for quantitative comparison in section 4.

.

Table 1 A summary of the high-redshift data. For each SN, the redshift, the Modified Julian Date (MJD), the epoch since B-band maximum light, the telescope, the instrument, the instrument setting, the exposure time, the signal-to-noise ratio (per 20 Å bin), the percentage of galaxy contamination and SN Ia sub-type are given. See text for details.

SN-name	Red-shift[a]	Date (MJD)	Days from[b,e] B-band Maximum	Instrument	setup	telescope	Exposure time (s)	S/N[c]	Galaxy[d] %	ID
SN 2001gy	0.511	52021.3	−7,5(1)	FORS1	300V grism + GG435	VLT-UT1	2400	11	20	Ia
SN 2002fd	0.279	52376.1	−7(3)	FORS2	300V grism + GG435	VLT-UT4	600	46	28	Ia-pec
SN 2000fr	0.543	51676.2	−5.5(1)	FORS1	300V grism + GG435	VLT-UT1	7200	21	16	Ia
SN 2001gw	0.363	52021.4	−1(3)	FORS1	300V grism + GG435	VLT-UT1	1200	8	19	Ia
SN 2001ha	0.58	52022.0	0(3)	FORS1	300V grism + GG435	VLT-UT1	3600	4	6	Ia
SN 2002gl	0.510	52413.1	0(3)	FORS2	300V grism + GG435	VLT-UT4	3000	9	23	Ia
SN 2001hc	0.35	52022.1	0(3)	FORS1	300V grism + GG435	VLT-UT1	1800	14	14	Ia
SN 2001gr	0.540	52021.0	2(3)	FORS1	300V grism + GG435	VLT-UT1	3600	5	57	Ia
SN 2002gi	0.912	52407.2	2(3)	FORS1	300I grism + OG590	VLT-UT3	7200	3	37	Ia
SN 2001gm	0.478	52021.3	5(3)	FORS1	300V grism + GG435	VLT-UT1	2400	3	28	Ia
SN 2001go	0.552	52021.3	5.6(1)	FORS1	300V grism + GG435	VLT-UT1	2400	5	13	Ia
SN 2002gk	0.212	52413.3	6(3)	FORS2	300V grism + GG435	VLT-UT4	900	34	66	Ia
SN 2001go	0.552	52027.1	9.5(1)	FORS1	300V grism + GG435	VLT-UT1	7200	10	19	Ia
SN 2001go	0.552	52058.1	29.5(1)	FORS1	300V grism + GG435	VLT-UT1	9000	4	53	Ia

[a]The redshift is quoted to three significant figures if it is determined from host galaxy lines, otherwise two.

[b]Uncertainties are quoted in parenthesis

[c]For a 20 Å bin element

[d]Estimated contribution of the host as percentage to the total flux.

[e]When the epoch is quoted with 2 days uncertainty it refers to that of the best matching template.

2.2. SN identification

The identification of low-redshift SN Ia relies primarily on the detection of the absorption feature at approximately 6150 Å due to Si II λ6355. At redshifts above z=0.5, this characteristic feature is redshifted beyond the wavelength range of most optical spectrographs and the classification of the supernova has to rely on spectral features that lie at bluer wavelengths (Lidman et al. 2005; Hook et al. 2005). Because of the low signal-to-noise ratio usually available in high-redshift supernova spectra, this approach is not always conclusive.

We can also use the spectra to identify spectral peculiarities among SNe Ia as those found in 91Taa-like or SN 1986G/SN 1991bg-like supernova. In Table 2, the characteristics of four wavelength regions for different types and sub-types of supernovae are schematically reported. Each spectral feature is qualitatively described as *strong*, *weak* or *absent* based on the absorption strength and *broad* or *narrow* based on the wavelength span. In the absence of a procedure that is based on quantitative measurements, this scheme helps in identifying the SN type and, in the case of SNe Ia, the sub-type.

2.3. SN 2002fd: A SN 1991T/SN 1999aa-like Supernova

SN 2002fd is the only supernova in our data set that clearly deviates from a "normal Ia" (see Table 2). Within the scheme described above, the spectrum of SN 2002fd is similar to the spectra of 91Taa-like supernovae. The spectrum of SN 2002fd (re-binned to 20 Å per pixel) is shown in Fig. 2 where it is compared to other well-known peculiar and normal SN Ia. The strength of the 'Ca II H&K' feature in SN 2002fd is between that of 91Taa-like and normal SNe. The 'Fe II' and 'S II W' regions are similar to those in SN 1999ac (Garavini et al. 2005). Given the low-redshift, Si II λ 6355 is also visible. This feature in SN 2002fd is intermediate in strength to that of the same feature in SN 1999aa and in normal SNe. From this qualitative analysis of the spectrum, we classify SN 2002fd as a peculiar 91Taa-like object with characteristics in between the extreme SN 1991T-like SNe and normal SNe e.g. SN 1994D most similar to SN 1999aa. In section 4.3, we show that the equivalent widths of the absorption features in SN 2002fd are also consistent with those found at low redshift for the 91Taa-like objects.

Finding SNe with spectral characteristics similar to those of SN 1999aa at the redshift of SN 2002fd is important. 91Taa-like supernovae appear to make up 20% of all supernovae observed at low-z (Li et al. 2001b) although this high peculiarity rate could be the result of the difficulty in classifying spectroscopically peculiar SN 1999aa-like SNe (see the discussion in Branch (2001)). Nevertheless, we should find some of these SNe at high-redshift. Li et al. (2001b) used a Monte-Carlo simulation to estimate that, in a magnitude-limited high-redshift supernova search, where 91Taa-like SNe suffer an additional extinction of 0.4 magnitudes, between 18.6% and 6% (for an age bias of +7 and −1 days respectively) of all high-redshift SNe should be 91Taa-like SNe.

The precise number depends on the details of the methods that are used in the search. Many 91Taa-like SNe may have

Table 2 A description of the spectroscopic features used to type SN at z ≥ 0.5. Four wavelength regions are selected for performing the SN typing. Each spectral feature, in these regions, is qualitatively described as *strong*, *evident*, *weak* or *absent* based on the absorption strength and *broad* or *narrow* based on the wavelength span.

Region Id	λ-Region Rest Frame[Å]	Normal Type Ia	91T/99aa-like	91bg/86G-like	Type Ib/c	Type II
'Ca II H&K'[g]	3550-3950	strong/broad	weak or absent/broad[a,b]	strong/broad	evident/broad[c]	absent
'Si II'[d]	3950-4100	evident/narrow[b]	weak[a,b]	absent	absent	absent
'Fe II'[e,f]	4600-5200	strong/broad	strong/narrow[a]	strong/broad	strong/broad	absent[h]
'S II W'	5200-5600	strong/narrow[a,b]	weak or absent[a]	strong/narrow[a,b]	absent	absent

[a] Before maximum light

[b] Around maximum light

[c] A few peculiar exceptions.

[d] Marks the beginning of the distinctive strong Ti II absorption feature in 91bg/86G-like SNe Ia.

[e] In Normal Ia characteristic line profile time evolution.

[f] Dominated by Fe III in pre-maximum spectra of 91T/99aa-like SNe Ia.

[g] Split minimum in some SNe Ia.

[h] In Type II SNe, the Hβ line lies on the blue side of the "FeII" region.

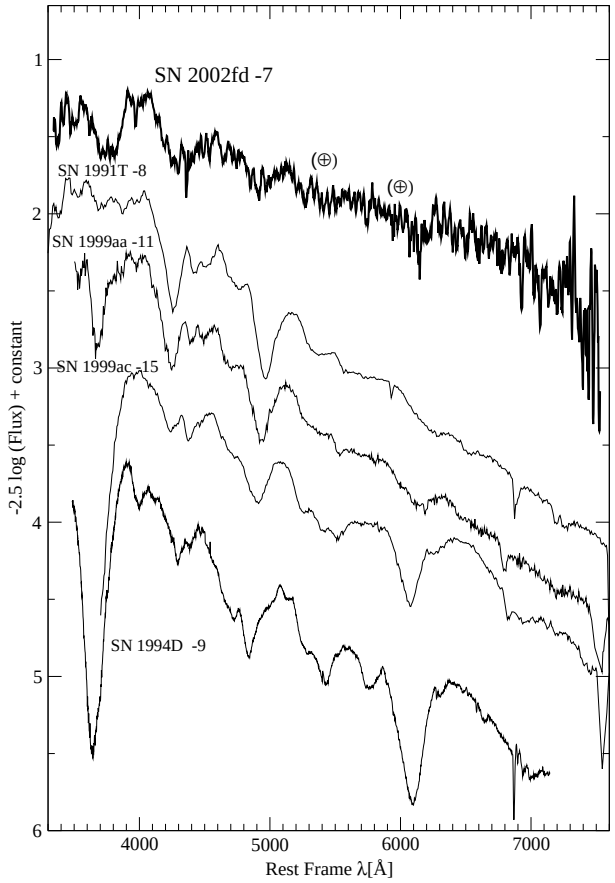

Fig. 2 SN 2002fd at day −7, re-binned to 20 Å per pixel (thick solid line), compared to normal and peculiar SNe. The ⊕ symbols mark regions of strong telluric absorption.

already been observed at high-redshift but not clearly identified because the signal-to-noise ratio in the spectrum was too low or the light-curve was not exceptionally broad. It is becoming clearer that 91Taa-like SNe do not always have broad light curves and vice-versa, see for example SN 1999ee (Hamuy et al. 2002), SN 2002cx(Li et al. 2003) or SN 1999aw (Strolger et al. 2002). SN 2002fd, for which we lack light curve information, is one of the first examples of a 91Taa-like supernova at high redshift, and its discovery demonstrates that these objects are found not only at low redshift. Of course, larger data samples are required to check whether the fraction of peculiar high-redshift SNe is consistent with that found in the low-redshift Universe or if there is an evolution with redshift in the relative fractions, which might affect the derivation of cosmological parameters from SNe Ia.

3. Equivalent Widths of Nearby Supernovae

During the photospheric phase, supernova spectral absorption features change in position, shape and strength. Supernova Type Ia show high homogeneity in their spectral energy distribution, but a certain degree of dissimilarity has been observed (see Filippenko (1997) for a review). In some cases the differences are dramatic resulting in the definition of SNe Ia subtypes. Few attempts have been tried to quantify such dissimilarities (see for example Benetti et al. (2005)) by means of spectral indicators. The analysis presented in this paper is devoted to quantitatively comparing spectral properties of local and distance supernovae. A new spectral indicator for SNe, i.e. equivalent width (EW), first described in Folatelli (2004), is introduced to carry out the comparison. In the following sections, we describe how we measure the EW of the broad absorption features in SN Ia spectra and we apply it to a sample of nearby SNe Ia.

3.1. Definition

In the case of supernova spectra the same definition of equivalent width as introduced in stellar spectroscopy can be used. However, the relationship between this quantity and the phys-

ical conditions of the ejecta is complex. In the expanding supernova envelope (and thus in a SN spectrum), it is not possible to identify a true continuum which is necessary to directly link the equivalent width to the element abundances. However, this does not prevent us from use this well-defined quantity and build a consistent set of measurements for all SNe in our datasets.

In this analysis we define an absorption feature as a wavelength region in the spectrum bounded by two local flux maxima. Fig. 3 shows these regions as we have defined for SN spectra at different epochs. Each feature is marked with a number from 1 to 8 and each number corresponds to a mnemonic name. The ranges over which the upper and lower limits of features are defined vary in time (because of the SN envelope expansion), and from SN to SN (i.e. SN spectral diversity). These limits are given in Table 3.

As already mentioned, in order to measure an EW, the continuum must be determined. We defined a pseudo-continuum as the straight line fit through the two local maxima that bound a feature[3] (see panel **(b)** in Fig. 3). A detailed explanation of the measurement technique is given in section 3.2

Once the continuum is traced, the EW is computed for each feature within its wavelength limits. The spectrum is divided by the continuum and the resulting area of the feature is measured (in units of Å). In this case, the calculation was approximated by a simple rectangular integration method:

$$\mathrm{EW} = \sum_{i=1}^{N} \left(1 - \frac{f_\lambda(\lambda_i)}{f_c(\lambda_i)}\right) \Delta\lambda_i, \qquad (1)$$

where λ_i ($i = 1, \ldots, N$) are the central wavelength values of bins of size $\Delta\lambda_i$ over the span of the feature; $f_\lambda(\lambda_i)$ is the measured flux in each bin i; $f_c(\lambda_i)$ is the fitted continuum flux evaluated at the same points. Deviating points due to bad pixels or narrow host-galaxy lines were rejected using a 3σ-clipping algorithm.

Table 3 Feature limits.

Feature ID	Mnemonic Label	Blue-ward limit range (Å)	Red-ward limit range (Å)
1	"Ca II H&K"	3500 – 3800	3900 – 4100
2	"Si II 4000"	3900 – 4000	4000 – 4150
3	"Mg II 4300"	3900 – 4150	4450 – 4700
4	"Fe II 4800"	4500 – 4700	5050 – 5550
5	"S II W"	5150 – 5300	5500 – 5700
6	"Si II 5800"	5550 – 5700	5800 – 6000
7	"Si II 6150"	5800 – 6000	6200 – 6600
8	"Ca II IR"	7500 – 8000	8200 – 8900

A 1σ statistical uncertainty was computed by error propagation from the estimated uncertainties in the spectral flux and in the pseudo-continuum:

$$\sigma_{\mathrm{EW}} = \left[\sum_{i=1}^{N} \left(\frac{\sigma_{f_i}^2(\lambda_i)}{f_c^2(\lambda_i)} + \frac{f_\lambda^2(\lambda_i)}{f_c^4(\lambda_i)}\sigma_{c_i}^2(\lambda_i)\right)(\Delta\lambda_i)^2\right]^{1/2}. \qquad (2)$$

By definition, the rest frame equivalent width is distance-independent and thus provides a useful tool for comparing spectra from different objects.

[3] The chosen maxima are those that maximize the wavelength span of the feature with the restriction that the derived continuum does not intersect the spectrum within the feature limits with the possible exception of noise artifacts in case of low signal to noise ratio data.

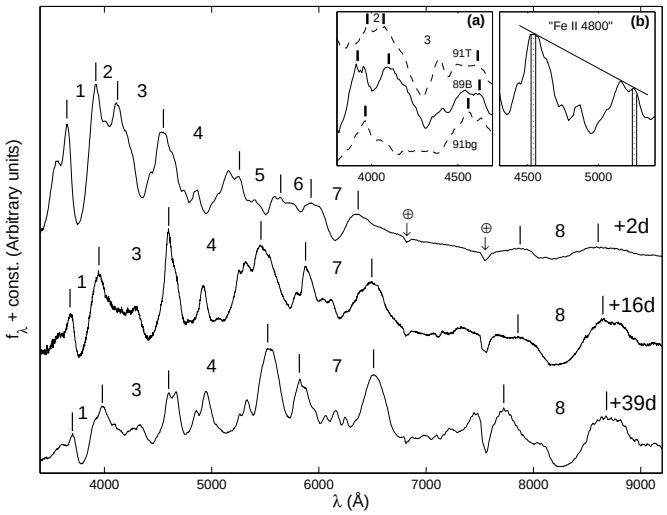

Fig. 3 SNe Ia spectral evolution and feature definitions for three epochs: 2, 16 and 39 days after maximum light. Numerical labels correspond to the following adopted feature names: **1**- "Ca II H&K"; **2**- "Si II 4000"; **3**- "Mg II 4300"; **4**- "Fe II 4800"; **5**- "S II W"; **6**- "Si II 5800"; **7**- "Si II 6150"; and **8**- "Ca II IR". Short vertical lines show the approximate positions where the continuum is taken in each case. Feature ranges change with time and, due to blending, some weaker features are not considered at later epochs. Note that, as the SNe leave the photospheric phase, continuum points correspond to emission peaks. *Panel* (**a**): the region of features #2 and #3 for near-maximum spectra of SN 1991T (top), SN 1989B (middle), and SN 1991bg (bottom). Feature #2 is not defined in the case of 1991bg-like SNe. Adopted feature limits are marked with vertical lines. *Panel* (**b**): an example of the continuum trace for "Fe II 4800" on a normal SN near the time of maximum light. Here, solid vertical lines show the regions where the continuum is fitted. Dotted lines mark the measurement limits.

3.2. Measurement technique

Measuring equivalent widths on high signal to noise ratio spectra is relatively simple since the local maxima bounding an absorption feature can be identified easily. On low signal-to-noise data the measurements can be more difficult. For comparing the results of high redshift supernova (generally of poor signal to noise) with those of local supposedly high quality SN spectra we have established a practical measurement technique (to be applied on spectra regardless to their signal to noise ratio) that minimize possible systematic effects.

To measure the EW of a spectral feature the local continuum must be determined. To perform this operation we proceeded as follows:

– The two local maxima that bound the absorption feature are visually identified and marked. These are the bounds used in performing the sum in Eqn. 1.
– A small wavelength region (to which hereafter we refer to as fitting region) is selected around each identified maximum[4], always within the wavelength ranges of Table 3.
– A straight line is fitted to the data in the fitting regions
– The result of the fit is taken as the continuum and used as an input in Eqn. 1.

The wavelength span of the two fitting regions depends on the morphology of the local maxima. On the blue end of the spectrum, where more absorption features are found, the maxima tend to be narrower than on the red end. Thus, the fitting regions are, on average, smaller (~ 20 Å) in the blue and slightly larger (~ 25 Å) in the red part of the spectrum. Larger wavelength spans would tend to set a lower continuum level and thus to produce EW systematically biased toward smaller values. The size of the fitting region is independent of the signal-to-noise ratios of the spectra; however, in low signal-to-noise ratio spectra noise spikes that could bias the continuum fit are avoided.

3.3. Data-set

Two different data sets are used to derive the properties of EW in local SNe.

Set A - 77 spectra from 13 of the SNe Ia discovered and followed by the Supernova Cosmology Project (SCP) in collaboration with members of the EROS (Hardin et al. 2000), QUEST (Schaefer et al. 1999), and Nearby Galaxies SN Search (Gal-Yam et al. 1999) teams. These SNe cover a range of redshift approximately of $0.01 < z < 0.15$.
The two-dimensional raw images were reduced according to standard procedures. The calibrated spectra were additionally corrected for atmospheric and Galactic extinction (Cardelli et al. 1989; Schlegel et al. 1998) and their flux-calibration was checked against measured broad-band photometry. The spectra were put in the SN rest-frame. More details about these data can be found in Table 4. All the spectra in **Set A** include estimated statistical uncertainties for each wavelength bin. A subset of these spectra showed some degree of host-galaxy light contamination, especially at late times. This contribution was estimated and subtracted (for details of the procedure see 2.1) in cases where it exceeded 10% of the total flux.

Set B - 89 published spectra from 8 well-observed, nearby objects. See Table 5 for a summary on these data, including the original sources and the redshifts used to put them in the rest-frame. Additionally, the spectra were tested and corrected when needed by use of available broad-band photometry. Given the absence of published uncertainties on these spectra, statistical errors were estimated from the point-to-point dispersion.

The epochs used in this analysis are based on light curve estimates. In the case of **Set A**, the date of maximum B-band brightness was determined using preliminary light curves. Therefore the epochs used to date the spectra were taken as the integer number of days since maximum light. The photometry data available for both sets were used to fit the template B-band light curve given by Goldhaber et al. (2001) and thus to obtain the values of $\Delta m_{15}(B)$ and stretch for each SN.

The two sets contain some peculiar SNe Ia, including the prototypes of the two subclasses: SN 1991T and SN 1991bg. SN 1999aa (Garavini et al. 2004), SN 1999aw (Strolger et al. 2002), and SN 1999bp (first analyzed in this work) are included in the 1991T-like subclass. All these SNe present values of the light curve-shape parameter $\Delta m_{15}(B) < 1.0$ ($s > 1.1$) and are thus slow decliners. On the other extreme, SN 1986G (Phillips et al. 1987; Cristiani et al. 1992) and SN 1999by (Vinkó et al. 2001; Garnavich et al. 2004) belong to the 1991bg-like subclass. These are fast decliner SNe, with $\Delta m_{15}(B) > 1.70$ ($s < 0.80$). The case of SN 1999ac (Garavini et al. 2005) is considered separately. This SN has photometric and spectroscopic peculiarities that make it a unique object: its light curve shows a slow rise similar to SN 1991T but a fast decline (Phillips et al. 2002) and its spectrum is similar to SN 1999aa.

3.4. Tests for Systematic Errors

Possible systematic errors arising from the choice of the regions at both sides of the feature where the pseudo-continuum is fitted were accounted for by randomly shifting these regions (typically within a quarter of the region size in each direction[6]) and computing the weighted root-mean square deviation (rms) of the encountered EW's. This source of error was added quadratically to the one given in Eqn. 2. This was the dominant source of uncertainties when the signal-to-noise ratio per resolution element was above ~10.

It is known that EWs can be affected by poor resolution or low signal-to-noise ratio of the spectra (see, for example Gray (1992)). These effects were tested as follows. Boxcar smoothing was used to decrease the resolution of the best-sampled spectra and reproduce the range of resolutions in the present data set. Due to the nature of the broad SN features, even the lowest resolution available (~10 Å/pixel) did not produce any significant change of the measured EW.

In the present spectra sample **Set A** and **Set B**, pixel-to-pixel signal-to-noise ratios ranged from about 5 to several hundred. When Gaussian noise was added to the best-quality spectra, in order to reproduce that quality range, no significant bias was detected on the resulting EW values.

Additionally, the effect of reddening was also tested by artificially adding it to several spectra up to a value of $E_{B-V} = 0.32$ (corresponding to $A_V = 1$ mag, with $R_V = 3.1$) following the law given in Cardelli et al. (1989). This produced no significant change in the resulting values for EW. The nature of these quan-

[4] See panel **(b)** in Fig. 3, the four vertical lines represent an example of the wavelength span of each fitting region.

[5] The NASA/IPAC Extragalactic Database (NED) is operated by the Jet Propulsion Laboratory, California Institute of Technology, under contract with the National Aeronautics and Space Administration.

[6] Considering the uncertainty on the location of a region of size l to be $l/\sqrt{12} \sim l/4$, as derived from the second moment of a uniform distribution.

Table 4 SNe from **Set A** (SCP data).

SN	z	Host Galaxy	Galaxy Type[a]	Observed Epochs[b]
1999aa	0.0144	NGC 2595	SAB(rs)c	−11, −7, −3, −1, 5, 6, 14, 19, 25, 28, 33, 40, 47, 51, 58
1999ac	0.0095	NGC 6063	Scd	−15, −9, 0, 2, 8, 11, 16, 24, 28, 31, 33, 39, 42
1999ao	0.054	Anon.	S:	5, 7, 10, 13, 18, 34, 40
1999au	0.124	Anon.	S:	12, 17
1999av	0.05	Anon.	E/S0:	2, 5, 9, 31
1999aw	0.038	Anon.	(?)	3, 5, 9, 12, 16, 24, 31, 38
1999be	0.019	Anon.	(?)	14, 19, 26, 33, 37, 44
1999bk	0.096	Anon.	E/S0:	4, 7, 9
1999bm	0.143	Anon.	S:	3, 6, 21
1999bn	0.129	Anon.	S:	2, 14, 22
1999bp	0.077	Anon.	S:	−2, 0, 1, 6, 17, 23
1999bq	0.149	Anon.	E/S0:	3, 18
1999by	0.0021	NGC 2841	SA(r)b	1, 6, 16, 27, 34

[a] Hubble type of the host galaxy. An entry followed by a colon is a classification based on the host galaxy spectrum. The rest are taken from NED[5]

[b] Rest-frame days since *B*-band maximum light.

Table 5 SNe from **Set B** (Public data).

SN	z ($\times 10^{-3}$)	Host Galaxy	Galaxy Type[a]	Epochs[b]	Sources
1981B	6.031	NGC 4536	SAB(rs)bc	0, 17, 26, 29, 35, 49	1
1986G	1.825	NGC 5128	S0 pec	−7, −5, −1, 0 ,3, 21, 28, 41, 44, 55	2
1989B	2.425	NGC 3627	SAB(s)b	−7, −5, −3, −2, −1, 3, 5, 8, 9, 11, 16, 18, 19	3
1990N	3.369	NGC 4639	SAB(rs)bc	−14, −7, 7, 14, 17, 38	4, 5, 6
1991bg	3.536	NGC 4374	E1	−2, 0, 13, 16, 23, 24, 30, 31, 44, 52	7, 8
1991T	5.791	NGC 4527	SAB(s)bc	−11, −9, −8, −7, −6, −5, −3, 0, 10, 15, 23, 24, 42, 45	9, 10, 11, 12
1992A	6.261	NGC 1380	SA0	−5, −1, 3, 7, 9, 11, 16, 17, 24, 28, 37, 46	13
1994D	1.49	NGC 4526	SAB(s)	−10,−9,−8,−7,−5,−3, 2, 4, 6, 8, 11, 13, 14, 16, 18, 20, 25	14, 15

[a] Hubble type of the host galaxy from NED[5].

[b] Rest-frame days since *B*-band maximum light.

Sources: (1) Branch et al. (1983); (2) Phillips et al. (1987); (3) Wells et al. (1994); (4) Leibundgut et al. (1991); (5) Phillips et al. (1992); (6) Mazzali et al. (1993); (7) Filippenko et al. (1992a); (8) Leibundgut et al. (1993); (9) Filippenko et al. (1992b); (10) Ruiz-Lapuente et al. (1992); (11) Phillips et al. (1992); (12) Jeffery et al. (1992); (13) Kirshner et al. (1993); (14) Meikle et al. (1996); (15) Patat et al. (1996).

tities, defined over a limited wavelength range, makes them insensitive to reddening.

Further systematic effects could arise from host-galaxy light contamination or other background sources which might not be well subtracted. The effect of additional signal underlying the SN spectrum would be to lower the values of EW. The published spectra from **Set B** in the present sample correspond to very bright, nearby SNe, for which SN and host-galaxy spectra can be resolved. For more distant SNe, from **Set A** and the high redshift data set, we used only the spectra where no significant contamination was found or when this could be reliably subtracted. We have tested this effect on a typical near-maximum light spectrum. Template galaxy spectra of Hubble types E and Sc were added to the SN spectrum in order to simulate contamination levels ranging from 0 to 50% of the total integrated flux between 3500 and 9000 Å. The EWs of all eight features were then measured on every spectrum. The decrease in the EW with increasing contamination levels was found to be approximately linear. Table 6 summarizes these results by giving the relative decrease of EW per each 10% of un-accounted contamination on the total integrated flux for both galaxy types. Since SNe Ia near maximum light are generally bluer than their hosts, errors in estimating the amount of host galaxy contamination leads to larger equivalent width errors for features at redder wavelengths. For early type galaxies, because of the presence of the Balmer break around 4000Å, the effect on the EW of "Ca II H&K" is less than 10% even for 50% contamination.

3.5. Results

Given the mean redshift of the high-redshift sample (z=0.49) and the typical S/N ratio of the spectra, we restrict our analysis to the bluest and strongest features - #4 "Fe II 4800", #3 "Mg II 4300" and #1 "Ca II H&K".

Table 6 The fractional decrease in the EW corresponding to a 10% increase in the amount of contamination from the host.

Feature ID	Mnemonic Label	Host Type E	Sc
1	"Ca II H&K"	0.019	0.080
2	"Si II 4000"	0.048	0.074
3	"Mg II 4300"	0.037	0.073
4	"Fe II 4800"	0.070	0.074
5	"S II W"	0.112	0.074
6	"Si II 5800"	0.128	0.066
7	"Si II 6150"	0.103	0.084
8	"Ca II IR"	0.155	0.114

3.5.1. "Fe II 4800" (#4).

Fig. 4 shows the evolution of the EW of feature #4 in nearby supernovae. The equivalent width increase constantly from before maximum up to three week after. The expansion of the ejecta and the consequently increasing optical depth are at the origin of this trend. At epochs later than 15 days, this feature has become broader as a consequence of the blending of lines lying to the red (see Fig. 3).

The number of data points enable us to compute a mean evolutionary curve for normal supernovae. The solid line in Fig. 4 shows this average curve represented as a cubic spline function. The curve was built in the range $-10\text{d} < \text{epoch} < 50\text{d}$ by dividing the epochs into 5 bins, calculating a weighted average of the EW in each bin, and finally tracing the spline function through those points. The coordinates (epoch,EW), in units of days and Å, of the 5 points defining the curve are: (-5,134); (5,181); (15,267); (25,339); (35,356).

The different subtypes of SNe Ia evolve approximately parallel to the mean curve. In general, 1991bg-like SNe lie above the curve and 1991T-like SNe lie below it. This is summarized in Table 7 which shows the distribution of the three SNe Ia subtypes with respect to the average curve. Column 1 lists the epoch bins in consideration. Column 2 gives the number of points from normal SNe in each bin. Column 3 lists the average EW for normal SNe and its 1-σ uncertainty. Column 4 shows the rms dispersion, which we name "δ", of normal SNe with respect to the average curve.

We note that for normal type Ia SNe the average trend in the first data bin is computed based on four data points from SN 1994D and one each from SN 1989B and SN 1990N. The mean is then biased toward the average EW value of SN 1994D between -10 and -6 days. This is higher than the measurement obtained on the other SNe, thus, the pre-maximum average trend has to be considered only indicative. More EW measurements are needed to firmly establish the normal pre-maximum SN behavior.

Columns 5 and 6 refer to 1991T-like SNe and show the number of points and the mean deviation from the average curve. Columns 7 and 8 show the same two quantities for the case of 1991bg-like SNe. The values in columns 6 and 8 are to be compared with δ. It can be seen that 1991T-like SNe show systematically negative deviations up to around a month after maximum light. The deviations are positive in the case of 1991bg-like SNe, although they are generally less significant —also, there are fewer data for this subtype.

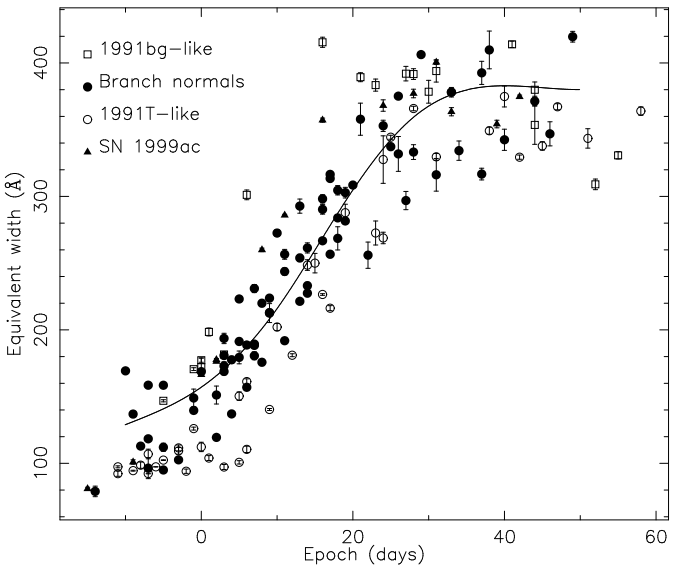

Fig. 4 Measured equivalent width values corresponding to "Fe II 4800" (#4). SN 1991bg-like objects are marked with open squares, 1991T-like SNe with open circles, normal SNe with filled circles and SN 1999ac with triangles. Error-bars are given by Eqn. 2 plus systematic uncertainties arising in the pseudo-continuum fit. The solid line shows a cubic spline function used to represent the average evolution of normal SNe in the sample, between days −10 and +50. In general, 1991bg-like SNe lie above the average curve whereas 1991T-like SNe lie below it.

3.5.2. "Mg II 4300" (#3)

Feature #3 is due to the contribution of various ions which varies with time. These include Mg II, Co II, Fe II, Fe III, and Si III for spectroscopically normal and 1991T-like SNe. In the case of 1991bg-like SNe, the region is dominated by strong lines of Ti II (Filippenko et al. 1992a; Mazzali et al. 1997). The equivalent width evolution of this feature is different than that of "Fe II 4800" as can be seen in Fig. 5.

The EW of the feature increases dramatically over a short period of time as it mergers with the neighboring "Si II 4000" feature (feature #3 in figure 5). Before and after this increase, the EW of this feature is approximately constant. The phase at which this increase takes place is highly dependent on the SNe sub-type. For 1991bg-like SNe Ia it seems to occur as early as 5 days before maximum light (the earliest spectrum of a 1991bg-like SN in our sample), while normal SNe show this behavior around one week after maximum light, and 1991T-like objects show it later than day +10. Thus, the EW of the "Mg II 4300" feature can be used to discriminate between different Type Ia sub-types.

We describe the average evolution of this feature with the function:

$$f(\boldsymbol{\theta}, t) = \frac{A}{e^{\frac{t_{br}-t}{\tau}} + 1} + B, \tag{3}$$

Table 7 Dispersion of "Fe II 4800" EW for the three SNe Ia subtypes. See text for details.

Epoch		Normal		1991T-like		1991bg-like	
bin	n	$\langle$EW$\rangle$ (Å)	δ (Å)	n	$\delta_{\rm EW}$ (Å)	n	$\delta_{\rm EW}$ (Å)
(1)	(2)	(3)	(4)	(5)	(6)	(7)	(8)
$[-10,-6]$	6	132 ± 11	28	5	-29 ± 3	0	···
$[-5,-1]$	6	114 ± 12	37	5	-36 ± 5	2	16 ± 4
$[0,5]$	12	164 ± 10	28	5	-62 ± 9	4	24 ± 7
$[6,11]$	15	200 ± 8	25	4	-58 ± 15	1	113[a]
$[12,18]$	15	265 ± 9	25	5	-47 ± 12	1	139[a]
$[19,27]$	10	316 ± 12	30	5	-34 ± 18	3	58 ± 8
$[28,40]$	9	353 ± 13	36	5	3 ± 9	3	37 ± 5

Columns: (1) Range of epoch bins in days; (2) Number of points for normal SNe; (3) Average EW for normal SNe; (4) Dispersion (rms) of normal SNe around the average curve[7]; (5) Number of points for 1991T-like SNe; (6) Mean deviation of 1991T-like SNe from average curve. Uncertainties do not include the computed dispersion of normal SNe Ia around the curve (δ); (7) Number of points for 1991bg-like SNe; (8) Mean deviation of 1991bg-like SNe from average curve. Uncertainties do not include the computed dispersion of normal SNe Ia around the curve (δ).

[a] Only one measurement, thus no uncertainty is given.

with parameters $\boldsymbol{\theta} = (A, B, t_{br}, \tau)$. The solid line in Fig. 5 shows the average curve for normal SNe Ia between days −10 and +30. Other SN subtypes show a parallel trend. Table 8 lists the dispersion of normal SNe around the average curve and the deviations of 1991T-like and 1991bg-like SNe from the same curve.

We note that for normal type Ia SNe at epoch before maximum light the data points distribution appears to be bi-modal. The high values of EW are those measured on SN 1989B (two data points in the first bin and three in the second one) and on SN 1990N (one data point in each bin). SN 1994D shows instead low EWs (two data points in each bin before maximum light) with SN 1992A measuring intermediate values (in both pre-maximum bins). The average trend is then greatly affected by SN 1994D which, as for feature #4, seems to be an outlayer. Because of the low statistics the pre-maximum trend has to be considered only indicative. An analysis including more normal type Ia SNe will be needed to asses the average trend and to investigate whether the apparent bi-modal distribution is a distinctive characteristic of type Ia SNe disclosing interesting supernova physics.

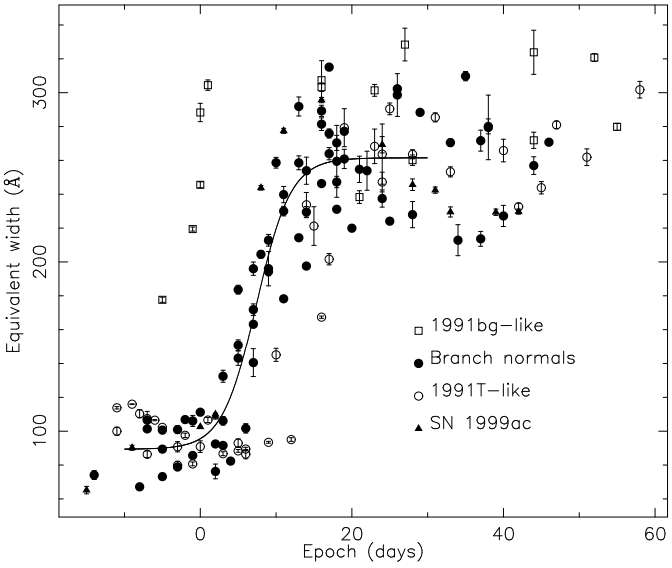

Fig. 5 Measured equivalent width values corresponding to "Mg II 4300" (#3). SN 1991bg-like objects are marked with open squares, 1991T-like SNe with open circles, normal SNe with filled circles and SN 1999ac with triangles. Error-bars are given by Eqn. 2 plus systematic uncertainties arising in the pseudo-continuum fit. The solid line represents the average behavior of normal SNe, fitted using the function of Eqn. 3. In general, 1991bg-like SNe lie above the average curve whereas 1991T-like SNe lie below it.

3.5.3. "Ca II H&K" (#1)

The prominent absorption trough found around 3800Å is attributed mainly to the H and K lines of Ca II with some contribution from Si II λ3858. Fig. 6 shows the change in the EW of this feature with phase. As expected for SN 1991T-like objects this absorption is particularly weak (and thuse has a low EW) expecially in the premaximum spectra. The intrinsic dispersion in EW values is greater than in the case of feature #3 and #4 and there is no trend with time. The evolutionary behavior is more or less peculiar to each object both qualitatively and quantitatively. The dispersion on EW is greater before maximum light, where some objects show an increase and others a decrease. After maximum light, there is normally a slow decrease, except for the 1991bg-like objects which maintain or increase their EW.

The two points with EW > 170Å after day 0 belong to SN 1999bm. Their large EW values are due to an unusually broad "Ca II H&K" feature. This phenomenon might be caused by the presence of a strong, high-velocity Ca II component, as suggested in the case of the Ca II IR triplet for SN 2001el (Wang et al. 2003). The signal-to-noise ratio of the spectra of

[7] In general we find $\delta \sim \sqrt{N} \cdot \delta_{\rm EW}$, but note that there are slight deviations due to the use of different epoch bins for this table and in building the average evolutionary curve.

Table 8 Dispersion of "Mg II 4300" EW for the three SNe Ia subtypes.See text for details.

Epoch		Normal		1991T-like		1991bg-like	
bin	n	$\langle$EW$\rangle$ (Å)	δ (Å)	n	$\delta_{\rm EW}$ (Å)	n	$\delta_{\rm EW}$ (Å)
(1)	(2)	(3)	(4)	(5)	(6)	(7)	(8)
$[-10,-5]$	6	90 ± 7	16	6	15 ± 4	0	···
$[-4,0]$	6	98 ± 5	14	5	-5 ± 3	4	139 ± 22
$[1,5]$	9	118 ± 12	28	4	-25 ± 12	1	206[a]
$[6,10]$	10	184 ± 14	26	4	-77 ± 12	0	···
$[11,17]$	15	251 ± 10	33	5	-69 ± 23	2	48 ± 2
$[18,30]$	15	257 ± 7	27	6	8 ± 6	4	21 ± 20

See column explanations in Table 7.

[a] Only one measurement, thus no uncertainty is given.

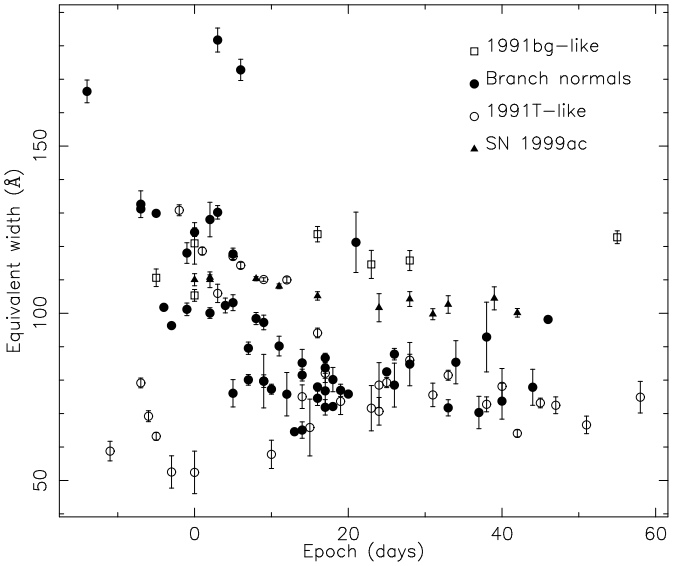

Fig. 6 Measured equivalent width values corresponding to "Ca II H&K" (#1). SN 1991bg-like objects are marked with open squares, 1991T-like SNe with open circles, normal SNe with filled circles and SN 1999ac with triangles. Error-bars are given by Eqn. 2 plus systematic uncertainties arising in the pseudo-continuum fit.

SN 1999bm in the region around 8000 Å is too low to determine the presence of such a component.

4. Comparing High and Low-redshift spectra

In this section, we compare our high-redshift spectra with the low redshift spectra described in section 3.5. The comparison is carried out by means of two spectral indicators:

1) the photosperic velocity of the Ca II H&K spectral line as derived from the minimun of the absorption features,

2) the equivalent width mesurements of "Ca II H&K", "Mg II" and "Fe II".

We first perform a qualitative analysis (sections 4.1 and 4.1.2) and then turn to a more quantitative approach (section 4.2). The measured values are reported in Table 9.

4.1. Velocities

For normal SNe Ia, the velocity of Ca II H&K drops rapidly, from values around 22000 km/s before maximum light to 14000 km/s at maximum light. After maximum light, the rate of decrease slows and the velocity decreases by about 4000 km/s in 50 days. The mean trend for normal SNe Ia, from 10 days before maximum light to 40 days after maximum light, is shown in Fig. 7. The shaded area represents the dispersion (one standard deviation about the mean). The trend and the dispersion have been computed from a large sample of nearby supernova (Garavini et al. 2004).

The inferred expansion velocity of the ejecta in underluminous SNe is lower than the expansion velocity in normal SNe (Leibundgut et al. (1993); Wells et al. (1994); Patat et al. (1996); Garnavich et al. (2004); Li et al. (2003)). The differences are more pronounced in the case of the Si II λ6355 absorption feature where differences of more than 2000 km/s are seen (Branch & van den Bergh 1993). The separation is less conspicuous for the Ca II H&K absorption — measurable in the redshift range of our data set — but the trend remains, as can be seen in Fig. 7 where SN 1999by (Garnavich et al. 2004) and SN 1991bg (Leibundgut et al. 1993) are plotted with the dashed and dotted lines, respectively. Assuming that intrinsically low-luminosity high-redshift SNe show the same spectral characteristics as those in the local Universe, measured expansion velocities values on the lower edge of the distribution shown in Fig. 7, would suggest a possible under-luminous SN.

The velocities of both the low-redshift and high-redshift SNe are individually measured by performing an error-weighted non-linear least-squares fit to the entire line profile manually selecting the end points limiting the wavelenght region where to perform the fit. The line profile is modeled with a Gaussian plus a linear component. This method accurately reproduce the absorption line profile and it has been succefully used in previous works (e.g. Garavini et al. (2005); Hook et al. (2005)). All the SNe in our data set were measured, with the exception of SN 2001gk, for which the line profile is incomplete, and SN 2001go at +29 days, for which the signal to noise is too low to correctly identify the absorption. The uncertainty in the redshifts is taken to be $\sigma_z = 0.001 \equiv \sigma_{cz} = 300\ km/s$ if the redshift was estimated from galaxy lines. For SN 2001ha and

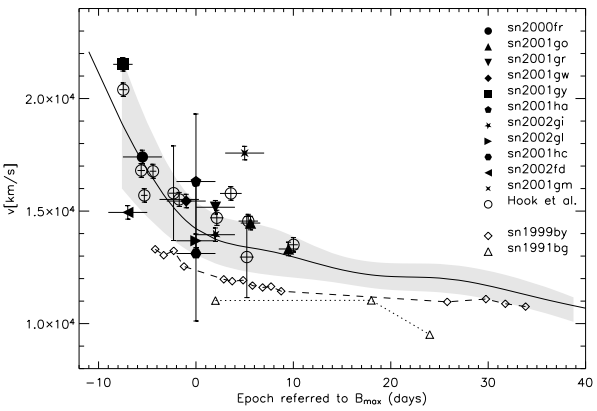

Fig. 7 The change in the velocity of the Ca II H&K feature with epoch for a sample of high-redshift SNe (presented in section 2, filled symbols, and from Hook et al. (2005) open circles) and a sample of low-redshift SNe. The dashed and dotted lines indicate the values of extremely under-luminous SNe SN 1999by (Garnavich et al. 2004) and SN 1991bg (Leibundgut et al. 1993) respectively. The solid line indicates the average trend for Ca II H&K, which has been computed using a large data set of low-redshift normal SNe Ia (Garavini et al. 2004). The gray band shows the dispersion (1 standard deviation) of the data about the average trend.

SN 2001hc, we could not identify host galaxy lines, so their redshifts were estimated by comparing their spectra with the spectra of nearby SNe Ia. In these cases the uncertainty is increased to $\sigma_z = 0.01 \equiv \sigma_{cz} = 3000\ km/s$. This uncertainty dominates the statistical uncertainty from the fit.

The velocity of the Ca II H&K feature in all our high-redshift supernovae lie above the dashed line in Fig. 7, which represents the velocity of this feature in the peculiar under-luminous SN 1999by. We note that the velocities of our high-redshift SNe are consistent with those of spectroscopically normal SNe. In Fig 7 open circles indicate the measurements reported in Hook et al. (2005) where a similar result was found in an independent sample of high redshift SNe Ia. We note that the two high-redshift supernova samples are consistent with each other. Li et al. (2001b) estimated that 16% of all supernovae discovered in the local Universe are under-luminous. However, as already mentioned in section 2.1 for magnitude-limited high-redshift supernova searches — such as those carried out by the SCP — there is a bias against discovering SN 1991bg-like SNe. Thus, the lack of any such SNe in our high-redshift SNe sample is not unexpected.

4.1.1. Equivalent Widths of Distant Supernovae: Possible systematic effects

Because of the required visual identification of the maxima in low signal to noise ratio data, different observers might tend to select fitting regions differing both in wavelength span and location. As for the measurements on low redshift SNe, possible systematic uncertainties arising from the selection of the region around each maximum were accounted for by Monte-Carlo simulations. Each identified fitting region was randomly varied in wavelength span according to a Gaussian distribution with $\sigma = l/4$, where l is the original span of the fitting region (typically $l = 20$ Å). Additionally, the wavelength of the region was randomly shifted according to a Gaussian distribution with $\sigma = 10$Å. This effect is insignificant for high signal to noise ratio data and thuse was not taken into account in section 3.4. The two effects were taken into account simultaneously. The sigmas of the simulations were chosen in a conservative manner so as to take into account even large mis-identification. The standard deviation of the measurements so obtained was taken as systematic uncertainty associated with the measured value (see sec. 4.1.2).

Further systematic effects could arise from the removal of the host-galaxy light contamination. As described in section 3.4 residual galaxy light underlying the SN spectrum would bias the EW measurements toward low values. An overcorrection of the SN spectrum for the host galaxy light would, instead, bias the EW measurements toward high values.

We tested the accuracy of the template matching technique used to estimate the host galaxy contamination. White Gaussian noise was added to a template SN plus host galaxy spectrum to match the signal-to-noise ratios in the data, and the resulting spectra were run into the subtraction code. The resulting estimate of the host galaxy contamination was found to be accurate at the level of 10% of the total flux. The corresponding systematic uncertainty in the EWS was computed accordingly to the values given in Table 6.

Other sources of systematic effects such as signal to noise ratio, reddening and spectral resolution do not differ from the case of nearby SNe and were already discussed in section 3.4. In particular, the resolutions of our VLT spectra are higher than those of the nearby data set and thuse we do not expect to be affected by limited resolution effects.

4.1.2. Equivalent Widths of Distant Supernovae: Measurements

In Figs.8, 9 and 10, we compare the strengths of "Fe II 4800", "Mg II 4300" and "Ca II H&K" absorption features in high redshift SNe spectra with those of local objects presented in section 3. Since the EWS of these features are a strong function of the phase, they are plotted with respect to B-band maximum light. Note, that the plotted errors bars in the EWS of the high-redshift SNe Ia include both statistical uncertainties, from the measurement, and systematic uncertainties from residual host galaxy contamination but do not include that from possible misidentification of the maxima around the absorption feature (i.e. misidentification of the fitting regions). Table 9 reports the measured EW values, their uncertainties are reported between parentheses. The first value in the parentheses includes only statistical and host galaxy contamination uncertainties, the second includes also the possible fitting region uncertainties added in quadrature.

In Fig 8 the comparison of the "Fe II 4800" EWS is shown. All SNe (with the exception of SN 2001gu, SN 2001gw, SN 2001gy and SN 2002gi, for which the absorption feature was not easily identifiable) were measured and were found to

Table 9 Measurements of the velocities of Ca II H&K and of the EWs of Ca II H&K, Mg II and Fe II. Measurements uncertainties are reported in parenthesis. The first value includes statistical plus host galaxy contamination uncertainties, the second value includes (added in quadrature) also the possible systematic uncertainties due to misidentification of the fitting regions, (see sec. 4.1.1 for details).

SN	day	Ca HK vel	Ca II H&K EW	Mg II EW	Fe II EW
sn2001gy	−7.5 (1)	21520 (300)	176 (8/21)	111 (12/31)	
sn2002fd	−7 (2)	14940 (300)	73.6 (3/14)	101 (8/11)	86 (15/23)
sn2000fr	−5.5 (1)	17400 (300)	122 (13/14)	103 (6/13)	91 (13/23)
sn2001gw	−1 (2)	15440 (300)	130 (9/13)	125 (17/22)	
sn2002gl	0 (2)	13680 (300)	124 (14/15)	121 (12/18)	168 (20/25)
sn2001ha	0 (2)	16310 (3000)	188 (19/22)	132 (9/24)	216 (33/62)
sn2001hc	0 (2)	13110 (3000)	112 (15/15)	116 (11/18)	140 (15/23)
sn2002gi	2 (2)	13950 (300)			
sn2001gr	2 (2)	15170 (300)	94.6 (10/22)	140 (16/34)	141 (31/69)
sn2001gm	5 (2)	17580 (300)	128 (23/26)	123 (17/40)	169 (34/84)
sn2001go	5.6 (1)	14470 (300)	120 (11/28)	93 (11/24)	191 (28/41)
sn2002gk	6 (2)		91 (6/11)	161 (14/16)	157 (16/17)
sn2001go	9.5 (1)	13320 (300)	112 (6/13)	181 (14/24)	174 (20/27)
sn2001go	29.5 (1)			228 (22/48)	315 (41/52)

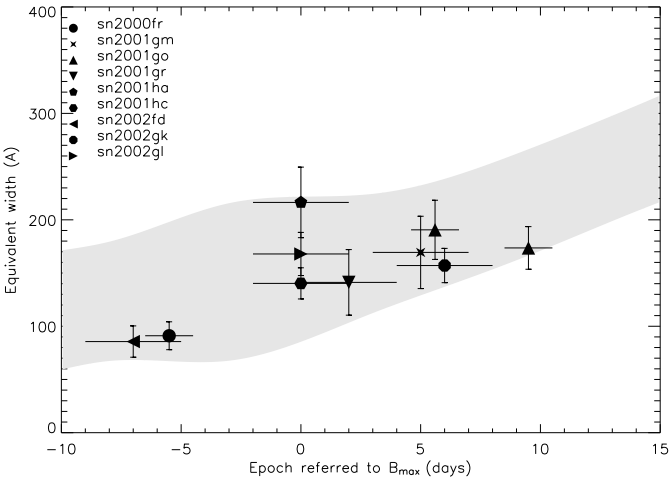

Fig. 8 A comparison between the 'Fe II 4800' EWs in low- and high-redshift SNe Ia. High-redshift supernova are indicated by large filled symbols. The gray filled area represents the 95% probability region for normal low-redshift SNe Ia as presented in section 3.5.

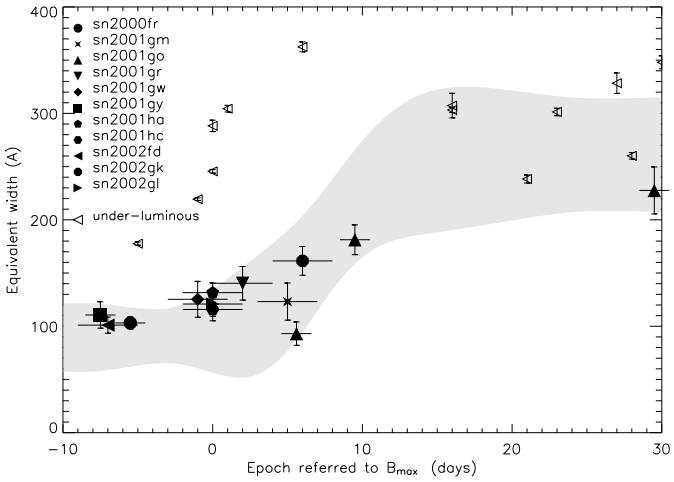

Fig. 9 A comparison between the 'Mg II 4300' EWs in low- and high-redshift SNe Ia. High-redshift supernova are indicated by large filled symbols. The gray filled area represents the 95% probability region for normal low-redshift SNe Ia as presented in section 3.5. Peculiar under-luminous SNe are shown separately for comparison.

be well within the 95% probability distribution of low-redshift supernovae indicated by the gray filled area.

Fig 9 shows that the "Mg II 4300" EWs of the high-redshift supernovae (all except SN 2002gi are measured) are consistent with the trend defined by the 95% probability distribution of low-redshift normal supernova indicated by the gray filled area. Moreover, SN 2001go, for which measurements at three epochs are available, shows the sudden increase at around one week after maximum, as do most low-redshift normal SNe.

Fig. 10 shows the comparison of the values of the EW of "Ca II H&K". For this feature, as described in section 3.5, it is not possible to identify a distinctive trend for SN subgroups as function of time. Before twenty days post-maximum normal and under-luminous low-redshift SNe populate the region spanning between EW=60 Å and EW=140 Å. In Fig. 10 the gray filled area represents the 95% probability region for normal (non-outlayers) and under-luminous low-redshift SNe Ia. Some outlayers are found among normal SNe and are indicated with small diamond symbols. The overall EW intrinsic spread of this feature is the largest of all the features analyzed in this work. Before maximum light, peculiar 91Taa–like objects show systematically low values, as indicated by the small square symbols. The high-redshift supernovae (all except SN 2002gi are plotted) do not show significant deviations with respect to the low-redshift sample shown in the plot, and SN 2002fd falls on the 91Taa-like trend as expected.

Lentz et al. (2000) claim that the strength of supernova absorption features should be affected by the drift toward lower metallicity progenitors, expected at high-redshift. We tested this hypotesis as follows. We measured the equivalent widths of the absorption features of the presented models and computed the standard deviation with respect to the one solar metallicity model. The dispersions so computed were found lower

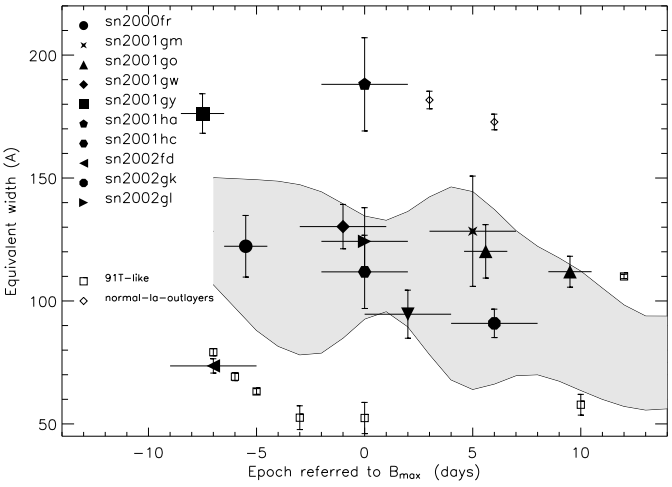

Fig. 10 A comparison between the 'Ca II H&K' EWs in low- and high-redshift SNe Ia. High-redshift supernova are indicated by large filled symbols. The gray filled area represents the 95% probability region for normal (non-outlayers) and under-luminous low-redshift SNe Ia. Outlayers normal SNe are indicated with the diamond symbols. Slow decliner SNe are indicated by the open square symbols.

than those measured in low-redshift supernovae data (reported in section 3). Thus, the spread in the EWs of nearby SNe Ia is dominated by other effects and not by metallicity variations as was modelled in Lentz et al. (2000). The possible change of rest frame U-B color in high redshift SNe is probably a more sensitive parameter for investigating the effect of the drift with redshift in the metallicity of SN progenitors.

4.2. Statistical comparison

In this section, a quantitative – statistical – comparison of the low- and high-redshift SNe is performed using the spectral indicators described in section 3. The mean trends in the EWs of the 'Fe II 4800' and 'Mg II 4300' features identified for normal – low-redshift – SNe can be used to test whether high-redshift supernovae EWs follow the same trends or show some differences.

The results of a set of χ^2 tests are shown in Table 10. The intrinsic dispersion around the models for normal low-z supernovae was added in quadrature to the statistical and systematic uncertainties to perform the test. The uncertainty on the time was propagated according to the EW model for normal low redshift SNe and added in quadrature to the measurements error on the EWs. The χ^2 test was repeated twice. Columns 1 to 4 in Table 10 report the result of the test when only the systematic uncertainty due to host galaxy subtraction was considered. Columns 4 to 8 report the result of the test when the possible systematic uncertainties due to misidentification of the maxima (i.e. fitting regions misidentification) was included. We note that the fitting region uncertainties — included in this second test — should be considered as upper limits to the possible systematic uncertainty due to the EW's measurement technique (see section 4.1.1 for details).

Columns 1, 2, 5 and 6 of Table 10 report the χ^2 referring to the comparison with the 'Fe II 4800' and 'Mg II 4300' EW models for normal supernovae, while columns 3, 4, 7 and 8 refer to the comparison with under-luminous SNe (e.g. SN 1986G and SN 1991bg). The hypothesis that the EW measured on our high-redshift supernovae follow the same behavior with lightcurve phase as those measured on low redshift normal supernovae is statistically accepted. Moreover, the hypothesis that EWs measured on our high-redshift supernovae are consistent with those of under-luminous SN 1991bg-like low redshift SNe is rejected.

4.3. The "Ca II H&K" EW of SN 2002fd

Prior to maximum light, the EW of Ca II H&K can be used to separate peculiar 91Taa-like SN Ia from normal SNe Ia, see Fig. 10. If the identification of SN 2002fd as a peculiar object is correct, we expect the EW to be lower than that of normal SNe. The average EW prior to light curve maximum in normal SNe is <EW> = 114.1 and the scatter around the mean value is $\sigma_{<EW>}$= 14.2 For peculiar 91Taa-like SNe we find <EW> = 68.7 and $\sigma_{<EW>}$ = 6.1 The value measured for SN 2002fd, (EW = 73.6 ± 2.9), is consistent — within one standard deviation — with that found for 91Taa-like SN Ia, and inconsistent (at more than 3 standard deviations) with the normal SNe Ia.

5. Summary and Conclusions

Spectroscopic data of 12 high-redshift supernovae, in the redshift interval z=0.212 to 0.912, were analyzed and a qualitative classification scheme was presented. Based on this classification scheme, all of our high-redshift SNe except one - SN 2002fd at z=0.27, which is similar to SN 1999aa, a perculiar SN Ia - were classified as normal SNe Ia. We also find, based on spectral properties alone, that none of the supernovae studied in this work are under-luminous. This is not unexpected because of the bias against selecting such objects in magnitude limited surveys.

A quantitative comparison between low and high-redshift SNe Ia by means of spectral indicators has been presented. The velocities of the ejecta in high-redshift supernovae, as inferred from the minimum of Ca II H&K feature, were compared to those of low-redshift SNe with the aim of uncovering differences. No differences could be found.

Using a low redshift SN Ia sample, we study the evolution in the EW of the strongest spectral features as a function of phase, and find that the EW of different SNe Ia sub-types (normal, 91T-like and 91bg-like) evolve differently.

The equivalent widths of "Fe II 4800", "Mg II 4300" and "Ca II H&K" in high-redshift SNe Ia are found to follow the same trends with epoch as those observed in low-redshift SNe. Furthermore, the equivalent widths of "Fe II 4800" and "Mg II 4300" in high-redshift SNe are found to be statistically consistent with the equivalent widths observed in low-redshift normal SNe.

The EWs of Ca II H&K in the spectrum of SN 2002fd are consistent with those observed in SN 1991T/SN1999aa-like objects in the local Universe quantitatively confirming the subtype identification of this SN and pointing out that this feature

Table 10 A statistical comparison of the equivalent widths (for features 'Fe II 4800' and 'Mg II 4300') of high-redshift SNe with the equivalent widths of normal (column 2, 3, 6 and 7) and under-luminous (columns 4, 5, 8 and 9) SN 1991bg-like low-redshift SNe. Columns 2, 4, 6,and 8 reports the χ^2 obtained with the number of degrees of freedom in parenthesis. Columns 3, 5, 7, and 9 report the probability to obtain a χ^2 value greater than that obtained. Columns 2 to 6 report the results including only the statistical and systematic uncertainties due to host galaxy subtraction. Columns 7 to 9 report the results when also the systematic uncertainty due to possible misidentification of fitting regions in included (see 4.1.1 and 4.2 for details).

Feature	$\chi^2_{\rm norm}$ (2)	$P_{\rm norm}$ (3)	$\chi^2_{\rm 91bg-like}$ (4)	$P_{\rm 91bg-like}$ (5)	$\chi^2_{\rm norm}$ (6)	$P_{\rm norm}$ (7)	$\chi^2_{\rm 91bg-like}$ (8)	$P_{\rm 91bg-like}$ (9)
Fe II	13.0(11)	0.29	29.6(11)	0.002	6.7(11)	0.8	16.8(11)	0.1
Mg II	11.2(13)	0.59	228.4(13)	0.00	7.3(13)	0.9	162.4(13)	0.00

can be successfully used to identify peculiar objects at high-redshift.

The number of supernova used in this analysis is small when compared to the numbers of SNe Ia that are now being observed. Both the ESSENCE and SNLS projects will result in samples of SNe Ia with similar spectral quality; however, the samples will be many times larger. With their strict selection criteria, they will be able to search for difference between low and high samples with more precission than what has been presented here.

References

Balland, C., Mouchet, M., Pain, R., et al. 2006, A&A, 445, 387
Barris, B. J., Tonry, J. L., Blondin, S., et al. 2004, ApJ, 602, 571
Benetti, S., Cappellaro, E., Mazzali, P. A., et al. 2005, ApJ, 623, 1011
Blakeslee, J. P., Tsvetanov, Z. I., Riess, A. G., et al. 2003, ApJ, 589, 693
Branch, D. 2001, PASP, 113, 169
Branch, D. 2003, astro-ph/0310685
Branch, D., Lacy, C. H., McCall, M. L., et al. 1983, ApJ, 270, 123
Branch, D. & van den Bergh, S. 1993, AJ, 105, 2231
Cardelli, J. A., Clayton, G. C., & Mathis, J. S. 1989, ApJ, 345, 245
Coil, A. L., Matheson, T., Filippenko, A. V., et al. 2000, ApJ, 544, L111
Cristiani, S., Cappellaro, E., Turatto, M., et al. 1992, A&A, 259, 63
Filippenko, A. V. 1997, ARA&A, 35, 309
Filippenko, A. V., Richmond, M. W., Branch, D., et al. 1992a, AJ, 104, 1543
Filippenko, A. V., Richmond, M. W., Matheson, T., et al. 1992b, ApJ, 384, L15
Folatelli, G. 2004, PhD Thesis U. Stockholm
Gal-Yam, A., Maoz, D., Strolger, L. G., et al. 1999, in International Astronomical Union Circular, 1–+
Garavini, G., Aldering, G., Amadon, A., et al. 2005, AJ, 130, 2278
Garavini, G., Folatelli, G., Goobar, A., et al. 2004, AJ, 128, 387
Garnavich, P. M., Bonanos, A. Z., Krisciunas, K., et al. 2004, ApJ, 613, 1120
Garnavich, P. M., Kirshner, R. P., Challis, P., et al. 1998, ApJ, 493, L53+
Goldhaber, G., Groom, D. E., Kim, A., et al. 2001, ApJ, 558, 359
Gray, D. F. 1992, Science, 257, 1978
Hamuy, M., Maza, J., Pinto, P. A., et al. 2002, AJ, 124, 417
Hardin, D., Afonso, C., Alard, C., et al. 2000, A&A, 362, 419
Hoeflich, P., Wheeler, J. C., & Thielemann, F. K. 1998, ApJ, 495, 617
Hook, I. M., Howell, D. A., Aldering, G., et al. 2005, AJ, 130, 2788
Howell, D. A., Sullivan, M., Perrett, K., et al. 2005, ApJ, 634, 1190
Jeffery, D. J., Leibundgut, B., Kirshner, R. P., et al. 1992, ApJ, 397, 304
Kirshner, R. P., Jeffery, D. J., Leibundgut, B., et al. 1993, ApJ, 415, 589
Knop, R. A., Aldering, G., Amanullah, R., et al. 2003, ApJ, 598, 102
Leibundgut, B., Kirshner, R. P., Filippenko, A. V., et al. 1991, ApJ, 371, L23
Leibundgut, B., Kirshner, R. P., Phillips, M. M., et al. 1993, AJ, 105, 301
Lentz, E. J., Baron, E., Branch, D., Hauschildt, P. H., & Nugent, P. E. 2000, ApJ, 530, 966
Li, W., Filippenko, A. V., Chornock, R., et al. 2003, PASP, 115, 453
Li, W., Filippenko, A. V., & Riess, A. G. 2001a, ApJ, 546, 719
Li, W., Filippenko, A. V., Treffers, R. R., et al. 2001b, ApJ, 546, 734
Lidman, C., Howell, D. A., Folatelli, G., et al. 2005, A&A, 430, 843
Matheson, T., Blondin, S., Foley, R. J., et al. 2005, AJ, 129, 2352
Mazzali, P. A., Chugai, N., Turatto, M., et al. 1997, MNRAS, 284, 151
Mazzali, P. A., Lucy, L. B., Danziger, I. J., et al. 1993, A&A, 269, 423
Meikle, W. P. S., Cumming, R. J., Geballe, T. R., et al. 1996, MNRAS, 281, 263
Patat, F., Benetti, S., Cappellaro, E., et al. 1996, MNRAS, 278, 111
Perlmutter, S., Aldering, G., della Valle, M., et al. 1998, Nature, 391, 51
Perlmutter, S., Aldering, G., Goldhaber, G., et al. 1999, ApJ, 517, 565
Phillips, M. M., Krisciunas, K., Suntzeff, N. B., et al. 2002,

From Twilight to Highlight - The Physics of Supernovae, ESO/MPA/MPE Workshop, Garching
Phillips, M. M., Phillips, A. C., Heathcote, S. R., et al. 1987, PASP, 99, 592
Phillips, M. M., Wells, L. A., Suntzeff, N. B., et al. 1992, AJ, 103, 1632
Riess, A. G., Filippenko, A. V., Challis, P., et al. 1998, AJ, 116, 1009
Riess, A. G., Strolger, L., Tonry, J., et al. 2003, astro-ph/0308185
Riess, A. G., Strolger, L.-G., Tonry, J., et al. 2004, ApJ, 607, 665
Ruiz-Lapuente, P., Cappellaro, E., Turatto, M., et al. 1992, ApJ, 387, L33
Schaefer, B. E., Snyder, J. A., Hernandez, J., et al. 1999, ApJ, 524, L103
Schlegel, D. J., Finkbeiner, D. P., & Davis, M. 1998, ApJ, 500, 525
Schmidt, B. P., Suntzeff, N. B., Phillips, M. M., et al. 1998, ApJ, 507, 46
Strolger, L.-G., Smith, R. C., Suntzeff, N. B., et al. 2002, AJ, 124, 2905
Tonry, J. L., Schmidt, B. P., Barris, B., et al. 2003, ApJ, 594, 1
Vinkó, J., Kiss, L. L., Csák, B., et al. 2001, AJ, 121, 3127
Wang, L., Baade, D., Höflich, P., et al. 2003, ApJ, 591, 1110
Wells, L. A., Phillips, M. M., Suntzeff, B., et al. 1994, AJ, 108, 2233